Cement & Concrete Composites 33 (2011) 411–423

Contents lists available at ScienceDirect

Cement & Concrete Composites

journal homepage: www.elsevier.com/locate/cemconcomp

Chemo-mechanical analysis of concrete cracking and degradation due to external sulfate attack: A meso-scale model

Andrés E. Idiart [a,*,1], Carlos M. López [b], Ignacio Carol [b]

[a] OXAND S.A., 49 Av. F. Roosevelt, 77210, Avon, France
[b] ETSECCPB (School of Civil Engineering), UPC (Technical Univ. of Catalonia), Campus Nord, Jordi Girona 1, Edif. D2, E-08034 Barcelona, Spain

ARTICLE INFO

Article history:
Received 10 March 2010
Received in revised form 3 December 2010
Accepted 4 December 2010
Available online 10 December 2010

Keywords:
External sulfate attack
Concrete
Chemo-mechanical modeling
Meso-scale

ABSTRACT

In this paper we focus on the external sulfate attack on concrete specimens at the meso-level. There is nowadays a renewed interest in rationally describing the mechanisms behind expansive processes leading to cracking and spalling of concrete exposed to sulfate solutions. A model is presented for degradation of concrete exposed to external sulfate attack at the meso-level, i.e. representing explicitly in the simulations the main heterogeneities of the material. A previously developed mesomechanical approach has been coupled with a diffusion–reaction analysis at the same scale. It is based on the systematic use of zero-thickness interface elements equipped with fracture-based constitutive laws, and the effect of discrete cracks on the transport of ions is explicitly accounted for. The main results obtained agree qualitatively and quantitatively well with experimental observations in terms of ettringite penetration depth, expansions, crack patterns and spalling effects.

1. Introduction

Durability of concrete has become a very relevant issue in structural design over the last decades. Significant progress has been achieved regarding our understanding of the chemistry behind the different degradation processes. However, our knowledge of the interaction of some of these processes and the resulting mechanical behavior is still limited. This is particularly the case in field situations, where generally two or more aggressive agents are present simultaneously, thus increasing the complexity of the mechanisms governing the deterioration of concrete structures. One practically relevant degradation process is the external sulfate attack, characterized by the ingress of sulfate ions from the surrounding medium, finally leading to expansions, cracking, spalling, and eventually to the complete disintegration of the material [26,38,42,45,49]. It is generally accepted that the cause of these expansions is the formation of ettringite from the sulfate ions and the different aluminate phases in the hardened cement paste. Even though this problem has been studied for a long time, the mechanisms by which sulfate ingress leads to overall expansions are not yet totally understood. Recent advances in the experimental [15,45] and also in the modeling fields [3,20] have shown encouraging results towards this goal. There is a renewed interest in rationally describing this deterioration process, which is mainly related to the need of assessing the durability of underground nuclear waste containments and tunnel linings, which may be sometimes in contact with sulfate-rich soils. The presence of cracks may play an important role, facilitating the ingress of the aggressive solution, and thus accelerating the degradation process.

Over the last decade, a considerable effort has been devoted to develop chemo-transport-mechanical models that can be used to predict the behavior of cementitious materials under external sulfate attack with controlled test conditions [3,5,6,38,43,46,48,52]. The common feature in all of these models is that they attempt to quantify the mechanical consequences of the degradation processes on the basis of a chemo-transport calculation of the main species involved and the relevant reaction products formed (i.e. ettringite and/or gypsum). However, only some of them perform a full tenso-deformational mechanical analysis [3,5,38,52], and none of them seems to explicitly account for the effects of opening cracks in facilitating ion diffusion and accelerating the overall degradation process, which is a relevant feature in real cases.

In this paper, a model that explicitly accounts for the meso-structure of concrete, previously developed for purely mechanical analyses, is extended to the domain of chemo-mechanical coupled problems. Some of the main features of the mechanical model are a nonlinear fracture mechanics-based crack propagation procedure, a sound representation of the localization process (from multiple distributed microcracks to single or few macrocracks), and an accurate prediction of concrete behavior under numerous different cases of mechanical loading, such as uniaxial tension and compression, biaxial test, Brazilian test, triaxial compression, and basic

* Corresponding author.
E-mail address: Andres.Idiart@upc.edu (A.E. Idiart).
[1] Formerly at ETSECCPB, UPC.

0958-9465/$ - see front matter © 2010 Elsevier Ltd. All rights reserved.
doi:10.1016/j.cemconcomp.2010.12.001

creep [9,10,11,13,14,27,29,30]. Extension to diffusion-based and coupled hygro-mechanical phenomena in the case of drying shrinkage in concrete specimens, explicitly considering the effect of cracks on moisture diffusion, has also been previously studied in [23,24,28].

There are some advantages of considering concrete as a two-phase composite in the sulfate attack problem, in which the main physical and chemical processes occur within the cement paste matrix, while aggregates remain generally unaltered. This specific feature is at the origin of the typical crack patterns observed not only in cases where the matrix expands, as in the present study, but also when the matrix shrinks, as in the case of drying shrinkage [24].

The coupled chemo-mechanical constitutive model presented in this paper is based on the original proposal by Tixier and Mobasher [52], which has been significantly modified and improved. It consists of a single-ion diffusion–reaction model and considers a simplified view of the problem. It is assumed that external sulfate attack can be analyzed with the diffusion of only the ingressing sulfate ions that then react with portlandite to form gypsum. The latter is assumed to react in turn with the calcium aluminate phases of the hardened cement paste to form ettringite (see Section 3.1). The secondary ettringite formed in this way is ultimately assumed to generate the volume expansions and be responsible for potential deleterious effects on the overall concrete composite. In this paper, the original description and modeling of these diffusion/reaction processes has been improved. In addition, the combination of this model, in the context of a coupled approach, with the meso-mechanical representation of concrete using zero-thickness interfaces for cracking, previously developed by the authors [13,29,30], will lead to a deeper understanding of the chemo-mechanical degradation of concrete, explicitly considering the effect of a random aggregate distribution and of the cracking process. In addition, the effect of cracks on the transport process is also accounted for in an explicit way, by the introduction of zero-thickness interface elements for the diffusion analysis [47]. To the author's knowledge, the model described in this work is the only one currently capable of performing simulations of external sulfate attack at the meso-scale, i.e. explicitly considering the main heterogeneities of the material, and considering the effect of cracking explicitly in the degradation process.

2. Mechanical behavior of concrete at the meso-level: modeling aspects

2.1. Geometry and mesh generation

The 2D geometry of the mesostructure is generated by a stochastic procedure based on the Delaunay/Voronoï tessellation theory [29]. The input data considered in this work consist of fundamental parameters related to the mix design (maximum aggregate size, volume fraction, and aggregate shape), as well as some other parameters for controlling the randomness of the generation process. Only the largest aggregate particles are explicitly represented, as shown in Fig. 1. In turn, the surrounding matrix considers the homogenized behavior of mortar plus smaller aggregates. This is motivated by the fact that the fracture process and failure in concrete are generally governed by the main heterogeneities in the material. Once the final particle distribution has been obtained, the geometry is meshed through a structured procedure for the continuum (see e.g. [10,23]), and the mesh is refined near the edges to be exposed to a concentration gradient.

Additionally, in order to represent the main potential crack propagation paths, zero-thickness interface elements are introduced *a priori* in all the aggregate–matrix contacts and also within the matrix, in some predetermined positions (Fig. 1b). The advantages and drawbacks of this type of mesostructural representation for concrete, as compared to other kind of meso-models for mechanical and coupled with diffusion-driven phenomena in 2-D, have been previously discussed elsewhere [13,23]. Extension to 3D in the case of purely mechanical loading has also been addressed in Caballero et al. [10,11].

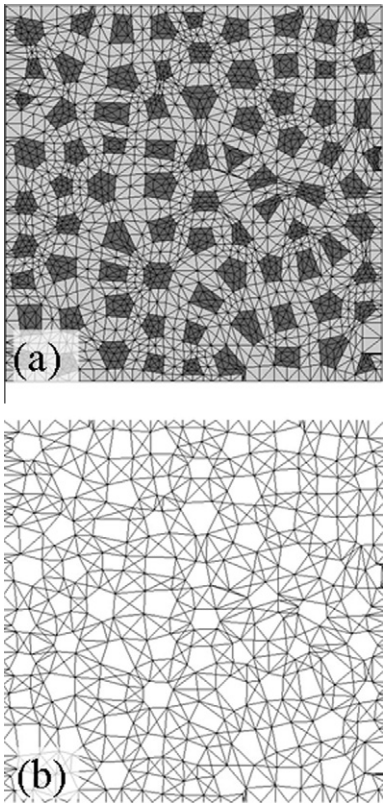

Fig. 1. FE discretization of a randomly generated geometry at the meso-level (a) and arrangement of zero-thickness interface elements for the same mesh (b).

2.2. Constitutive law with aging for interface elements

The constitutive law for the interface elements is based on the model previously proposed in (Carol et al. [12]). It also incorporates time as a variable to simulate the aging effect. The model is formulated in terms of the normal and tangential stress components in the mid-plane of the element $\boldsymbol{\sigma} = [\sigma_N, \sigma_T]^t$ and the corresponding relative displacements $\mathbf{u} = [u_N, u_T]^t$ (t = transposed). The constitutive relation conforms to work-softening elasto-plasticity, in which plastic relative displacements can be identified with crack openings. The initial failure surface $F = 0$ is given as a three-parameter hyperbola (tensile strength χ, asymptotic "cohesion" c, and asymptotic friction angle $\tan\phi$, curve 0 in Fig. 2), given by

$$F = \sigma_T^2 - (c - \sigma_N \cdot \tan\phi)^2 + (c - \chi \cdot \tan\phi)^2 = 0 \tag{1}$$

When cracking starts, the loading surface begins to shrink (curve 2 in Fig. 2). This is achieved by means of softening laws in which the surface parameters are functions of the work spent in fracture processes, denoted as W^{cr}. In order to control the evolution process of F, the model incorporates two parameters that represent the classical fracture energy in Mode I, G_F^I (pure tension) and a second energy under Mode IIa, denoted as G_F^{IIa} (defined under shear and high compression, so that dilatancy is eliminated), with values generally much higher than its Mode I counterpart. Under pure tension, the loading surface shrinks and moves to become another hyperbola with vertex at the coordinate origin. Under

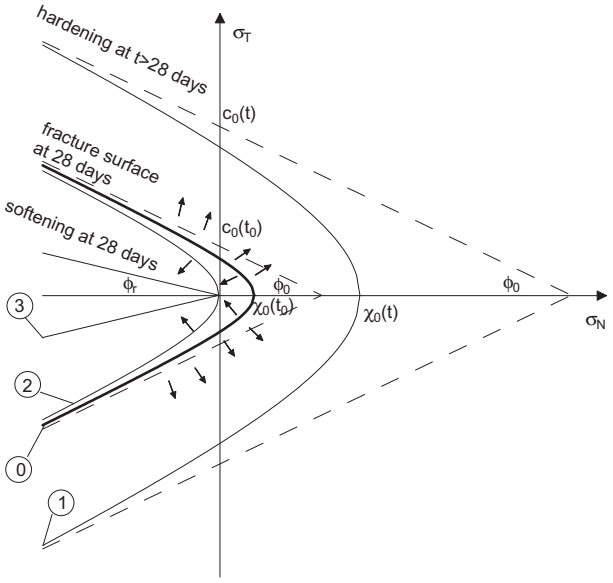

Fig. 2. Cracking surface considering the aging effect: evolution with time, and degradation due to energy spent in fracture.

mixed-mode, it degenerates further, asymptotically becoming a pair of straight lines (curve 3 in Fig. 2), representing the residual pure friction after all crack surface roughness has been eliminated.

The aging effect (increase of strength over time) may be considered in a phenomenological way through the evolution of the main parameters of the fracture surface (χ, c) with time, as well as the fracture energies G_F^I and G_F^{IIa}, through the following monotonic increasing function of the exponential asymptotic type:

$$f(t) = A \cdot f(t_0) \cdot \left[1 - \exp\left(-k \cdot (t/t_0)^p\right)\right], \quad \text{with } A = \frac{1}{1 - \exp(-k)} \tag{2}$$

In the previous equation, t is the age of the material and t_0 the reference age (usually 28 days), $f(t)$ and $f(t_0)$ are the values of the parameter considered at times t and t_0, respectively, and p and k are two shape parameters defining the s-shape of the curve and the relation between the asymptotic and reference values of the parameter, respectively. As a result, the initial fracture surface will expand in time (from curve 0 to curve 1 in Fig. 2).

The consideration of the aging effect causes the model to exhibit two counteracting effects: on one side the contraction of the fracture surface is determined by the energy spent in the fracture process, leading to softening behavior; on the other hand, the evolution of the main parameters in time results in an expansion of the fracture surface. This leads to a much richer behavior of the joint element, since the updated fracture surface will depend on the resulting combination of the loading state and the time interval considered.

In the case that aging is not considered, the parameter values of the interface constitutive model are chosen so that the sample's uniaxial compression and/or tension curves fit the experimental ones. In the case that aging is considered, the parameters in Eq. (2) are set so that the uniaxial compression and/or tensile strength at different ages fit the experimental values. A constitutive verification of the model response, as well as a more detailed description of the formulation, may be found in [23,24].

2.3. Aging viscoelasticity for the continuum matrix phase

In order to allow the simulation of the time-dependent deformations in concrete at the meso-level, a basic creep model for the matrix phase needs to be introduced while aggregates are assumed to remain linear elastic and time-independent. The rheological model which has been implemented, based on the work by Bazant and Panula [7], consists of an aging Maxwell-chain, which is equivalent to a Dirichlet series expansion of the relaxation function $R(t, t')$, dual to the usual compliance function $J(t, t')$ (t' = age at loading). Because the matrix exhibits a time-dependent mechanism while the aggregates do not, the parameters of the Maxwell-chain for the matrix have to be generally identified in order to reproduce the desired overall viscoelastic behavior corresponding to the concrete material [27]. If no other data is available than the elastic modulus at a reference time (usually 28 days), as in the case presented in Section 4.3, this adjustment may be performed with respect to the compliance function $J(t, t')$ given by a code formula. In the present study, this adjustment is made so as to fit the creep compliance function $J(t, t')$ given in the Spain concrete design code [19].

3. Description of the chemo-transport model

3.1. Chemical reactions involved

The most relevant chemical reactions that are generally accepted to potentially take place during the exposure to a sodium sulfate (Na_2SO_4) solution are now summarized (see e.g. [17,35,49,52]). In a first step, gypsum ($C\bar{S}H_2$) precipitates from the reaction between portlandite (CH) and/or calcium silicate hydrates (C–S–H), and the ingressing sulfates:

$$\begin{aligned} &CH + Na_2SO_4 + H_2O \rightarrow C\bar{S}H_2 + 2NaOH \\ &C{-}S{-}H + SO_4^{2-} + H_2O \rightarrow C\bar{S}H_2 \end{aligned} \tag{3}$$

Decalcification of C–S–H leads to important changes in the mechanical properties of cement paste. However, this is only likely to happen at very high sulfate concentrations, which is rarely the case in field conditions. The consideration of the later reaction would require a more sophisticated mechanical model, and has been left out of the present work. Therefore, the model is best suited to analyze moderate-to-high sulfate concentrations situations.

The second set of reactions consists of the formation of ettringite from monosulfoaluminate ($C_4A\bar{S}H_{12}$) (Eq. (4a)), unreacted tricalcium aluminate (C_3A) grains (Eq. (4b)), tetracalcium aluminate hydrate (C_4AH_{13}) (Eq. (4c)), and alumino-ferrite phase (C_4AF) (Eq. (4d)), although this last reaction seems to take place at a lower rate than the preceding ones (see for instance [44]):

$$\begin{aligned} &C_4A\bar{S}H_{12} + 2C\bar{S}H_2 + 16H \rightarrow C_6A\bar{S}_3H_{32} \\ &C_3A + 3C\bar{S}H_2 + 26H \rightarrow C_6A\bar{S}_3H_{32} \\ &C_4AH_{13} + 2CH + 3\bar{S} + 17H \rightarrow C_6A\bar{S}_3H_{32} \\ &3C_4AF + 12C\bar{S}H_2 + xH \rightarrow 4\left(C_6A\bar{S}_3H_{32}\right) + 2[(A,F)H_3] \end{aligned} \tag{4}$$

The presence of gypsum in addition to ettringite may be important at high sulfate concentrations, as in the case of laboratory samples exposed to high sulfate concentrations [34,41], but its presence in field conditions, under low sulfate concentrations, is rather questionable [32]. Gypsum formation is sometimes considered to be the cause of loss of cohesion of the cement paste as a result of decalcification of the C–S–H phase [38,48]. However, its participation in the observed overall expansion is still not clear [51] and will not be further considered in this study.

In the present model, following [5,52], it is assumed that the ingressing sulfates first react with portlandite to form gypsum (Eq. (3)). Thereafter, sulfates (now in the form of gypsum) react with the different non-diffusing aluminate phases of cement paste to form ettringite (Eq. (4)).

3.2. Transport model: a diffusion–reaction approach

The preceding chemical reactions take place according to the sulfates and calcium aluminates availability in time and space. In the original proposal [52], this was achieved by using a diffusion equation for the ingressing sulfate ions with a second-order reaction term for the precipitation of ettringite. In order to simplify the numerical treatment, it was proposed to lump all the chemical reactions that lead to ettringite precipitation in a single expression, as

$$C_{eq} + q \cdot \overline{S} \rightarrow C_6A\overline{S}_3H_{32} \tag{5}$$

where $C_{eq} = \gamma_1 C_4AH_{13} + \gamma_2 C_4A\overline{S}H_{12} + \gamma_3 C_3A + \gamma_4 C_4AF$, and $q = 3\gamma_1 + 2\gamma_2 + 3\gamma_3 + 4\gamma_4$, representing the stoichiometric weighted coefficient of the sulfate phase. Coefficients γ_i are defined as the proportion of each aluminate phase to the total aluminate content:

$$\gamma_i = C_i \left(\sum_{i=1}^{4} C_i \right)^{-1} \tag{6}$$

in which C_i (mol/m^3 of material) is the molar concentration of each aluminate phase per unit volume of solid material.

By introducing this lumped reaction, the system of equations regarding the diffusion–reaction process for the sulfate concentration, hereafter denoted as U (mol/m^3 of material), and calcium aluminate depletion yields

$$\frac{\partial U}{\partial t} = \frac{\partial}{\partial x}\left(D_U \frac{\partial U}{\partial x} \right) - k \cdot U \cdot C_{eq} \tag{7}$$

$$\frac{\partial C_{eq}}{\partial t} = -k \cdot \frac{U \cdot C_{eq}}{q} \tag{8}$$

where D_U (m^2/s) is the diffusion coefficient for sulfate ions through the porous network, C_{eq} (mol/m^3 of material) represents the equivalent lumped concentration of the reacting calcium aluminates, k (m^3/(mol s)) is the lumped rate of take-up of sulfates, and t (s) and x (m) are the time and space coordinate, respectively.

This formulation implies the use of a single reaction rate coefficient k for all the reactions, i.e. the same kinetics for all the reactions. In the present model, it is proposed to optionally treat the reactions separately, thus allowing the consideration of different kinetics for each reaction individually. To this end, additional equations for the depletion of the different ith calcium aluminate phases (C_i (mol/m^3 of material)) are introduced as

$$\frac{\partial C_i}{\partial t} = -k_i \cdot \frac{U \cdot C_i}{a_i} \quad \text{for } i = 1, n \tag{9}$$

so that Eq. (7) is rewritten as

$$\frac{\partial U}{\partial t} = \frac{\partial}{\partial x}\left(D_U \frac{\partial U}{\partial x} \right) - U \cdot \sum_{i=1}^{n} k_i C_i \tag{10}$$

where k_i (m^3/(mol s)) are the rates of take-up of sulfates, a_i are the stoichiometric coefficients for sulfates (in the form of gypsum) of the individual reactions, and n is the number of reactions considered. The consideration of different kinetics for each reaction adds $(n-1)$ equations to the system. In the particular case of implementation into a FE code, the (non-diffusing) variables C_i are considered as internal variables, which can be explicitly integrated, and only the sulfate concentration is considered as nodal variable [23]. In this improved version of the model, the relative proportions of the different aluminate phases γ_i (Eq. (6)) need not to remain constant in time throughout the simulation, but will generally depend on the difference between the rates of reaction k_i. It may be argued that the kinetics of the individual reactions for the formation of ettringite is often not known *a priori*. In those cases, the simplified version with a lumped reaction is still applicable, and the single kinetic rate k would have to be determined by inverse analysis.

Additionally, the transport of ions through the cracks is explicitly considered in the model with the discrete crack approach (Section 2). This has previously required the development of double-noded interface elements also for the transport analysis [47]. As a first approximation, it has been considered that no ettringite precipitation occurs within the cracks. In this way, the mass conservation equation within a discontinuity filled with an incompressible fluid, with a sulfate concentration U_{mp} (mp = mid-plane of the crack), and neglecting the variation in crack width (u (m)) within an infinitesimal time increment, may be written as [23,47]

$$-\frac{d\widehat{J}_l}{dx} + q^- + q^+ = 0 \text{(a)}, \quad \text{with } \widehat{J}_1 = u \cdot J_1 = -u \cdot D_U^{cr} \frac{dU_{mp}}{dx} = \widehat{D}_U^{cr} \frac{dU_{mp}}{dx} \text{(b)} \tag{11}$$

where $\widehat{J}_l$ is the longitudinal local transport rate, q^- and q^+ are the leak-off terms, incoming from the surrounding porous medium, $\widehat{D}_U^{cr}$ (m^3/s) is the diffusion coefficient through the cracks, and x is the coordinate along the crack axis. Note that by plugging in Eq. (11b) into (11a), a diffusion equation in terms of ionic concentration gradient is obtained.

The implementation of the diffusion–reaction model through the continuum has been verified with some simplified cases (as in [52]) having an analytical solution in [23,47].

3.3. Diffusion coefficient for sulfate ions

One of the advantages of the present mesostructural model is that the effective diffusion through the matrix can be explicitly split into the behavior through the uncracked porous matrix, and the diffusion through the cracks. In this work, the diffusion coefficient of the sound porous media is assumed to be dependent on the pore filling effect (the diffusivity decreases as pores are filled with precipitated species). The additional diffusion through the cracks is explicitly considered with the insertion in the FE mesh of zero-thickness interface elements also for the diffusion analysis (Section 3.3.2). In this way, the model accounts for the decrease in diffusivity due to the pore filling effect simultaneously with an increase of the effective overall diffusivity due to cracking and spalling phenomena.

3.3.1. Uncracked porous medium

Different models have been proposed in the literature to introduce the pore filling effect (e.g. [21,22,39]). In the present study, a hyperbolic function has been adopted, which yields comparable trends to the relationship proposed in [39], and which has the advantage of explicitly depending on the initial porosity (Φ_{ini}). Accordingly, the diffusion coefficient is calculated as

$$D_U(\Phi_{cap}) = D_0 + (D_1 - D_0) \cdot f(\beta_D, \Phi_{cap}) \tag{12}$$

$$\text{where} \quad f(\beta_D, \Phi_{cap}) = \frac{\exp(-\beta_D)\xi}{1 + (\exp(-\beta_D) - 1)\xi}, \quad \text{with}$$

$$\xi = (\Phi_{cap}/\Phi_{ini}) \tag{13}$$

In Eqs. (12), (13), Φ_{cap} represents the updated porosity value considering its reduction due to precipitation of secondary species, and β_D is a shape factor. Note that with the use of the previous expression the pore clogging does not necessarily yield a zero diffusion coefficient, as in other proposals (see e.g. [22]). Instead, it depends on the value of D_0 adopted (see [23]). This implies that a part of the diffusion process may occur through the gel (or nano) pores, which have been suggested to be interconnected (see e.g. [4]). The initial capillary porosity is calculated through a classical Powers' model, given by

$$\Phi_{ini} = v_c \cdot \left(\frac{w/c - 0.36.\alpha}{w/c + 0.32} \right), \quad \text{if } w/c > 0.36.\alpha \text{ (and 0 otherwise)} \tag{14}$$

where v_c (m^3/m^3 of material) is the volumetric fraction of cement in the solid, w/c is the water-to-cement ratio, and α the degree of hydration. The updated porosity value considers the decrease due to the precipitation of ettringite in the pores through the following expression:

$$\Phi_{cap} = \Phi_{ini} - \alpha_s C_{eq}^{react}, \quad \text{if } \alpha_s C_{eq}^{react} < \Phi_{ini} \text{ (and 0 otherwise)} \qquad (15)$$

The meaning of the term $\alpha_s C_{eq}^{react}$ is detailed in Section 3.4. It accounts for the volume of the reaction products that deposit within the cement paste.

3.3.2. Diffusion through the cracks

The effect of cracks on the ion transport is explicitly considered *via* the zero-thickness interface elements. This effect may be of importance, e.g. for determining penetration fronts in a more accurate way. Moreover, in the cases where spalling occurs, a drastic change in the boundary conditions of the chemo-transport analysis is expected to occur, thus accelerating the degradation process. Nevertheless, this important feature has not been given a lot of attention in the models proposed so far, mainly due to the complexity of introducing this aspect in the calculations, but also due to the fact that the existing models do not predict the crack patterns and the spalling effect accurately.

To consider the influence of cracks, a relation between crack width and its diffusivity must be introduced. In this regard, recent experiments have been carried out elsewhere in concrete samples to determine the diffusivity of chloride ions through cracked concrete [18]. In that work, a classical chloride migration test setup with artificially produced traversing cracks in the cylindrical samples (through an indirect tensile test), were used. They concluded that the relation between diffusivity and crack opening is linear until a crack width of around 100 μm (being κ_{cr} (m/s) the proportionality coefficient). Beyond this threshold, the diffusivity remains constant and approximately equal to the diffusivity in free solution.

For the implementation of the above relation within the framework presented in the previous section (Eq. (11)), the previous diffusion coefficient is multiplied by the crack width u (m), in order to relate the total transport through a discontinuity with the concentration gradient. As a result, a quadratic law of the diffusivity in terms of the crack width is obtained until the threshold crack opening is reached, after which the diffusion coefficient increases linearly with the crack width, as shown in Fig. 3. It is assumed here that the diffusivity increases with the square of u (m) between zero and a critical crack aperture (u_{crit} = 100 μm), as inferred from the tests. For larger crack openings, the diffusivity is considered to be proportional to u (m), the slope being the diffusion coefficient in free solution (D_{free} (m^2/s)). This may be written as:

$$\widehat{D}_U^{cr}(u) = \kappa_{cr} \cdot u^2 \ (m^3/s), \quad \text{if } u < u_{crit} = 100\ \mu m \qquad (16)$$

$$\widehat{D}_U^{cr}(u) = \kappa_{cr} \cdot u_{crit} \cdot u \ (m^3/s), \quad \text{if } u \geqslant u_{crit} \qquad (17)$$

where $\kappa_{cr} \cong D_{free}/u_{crit} \cong 1 \times 10^{-5}$ (m/s). There seems to be no such an experimental study for the diffusion of sulfate ions through cracked concrete specimens, although it could be expected that the main conclusions drawn for the chlorides diffusion are applicable to the sulfates case, since the diffusivities in free solution are similar for both types of ions: around 1.2×10^{-9} (m^2/s) for chloride ions and 1×10^{-9} (m^2/s) for sulfate ions SO_4^{2-} (see e.g. [40]). However, more research would be needed to confirm this hypothesis. In this paper, as a first approximation, the above described quadratic–linear relation has been implemented. A comparison of the model response when assuming different crack width – diffusivity relations may be found in [23].

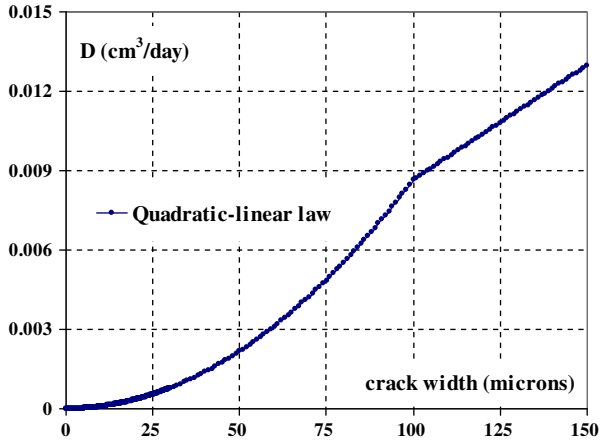

Fig. 3. Relation between the diffusion coefficient and the crack opening for the zero-thickness interface elements used in the simulations.

3.4. Calculation of volumetric expansions and coupling scheme

The origin and mechanisms of the observed overall expansions of concrete during external sulfate attack are, up to now, still controversial. It is fairly well accepted that ettringite is the main, if not the only, cause for these expansions. However, the mechanism by which the precipitation of ettringite leads to expansion, cracking and failure of concrete is yet not very clear (a complete review may be found in [8]). Most of the models proposed in the literature (for a summarized review see [23]) consider ettringite as the only responsible for the expansive process. Regarding the mechanism, mainly two directions have been followed. On one hand, some researchers consider the precipitation of crystals in a supersaturated pore solution, leading to a crystallization pressure exerted on the pore walls, which can be estimated through chemical thermodynamics [3,20,37]. This crystallization pressure has then to be upscaled for its introduction into a macroscopic analysis [3]. It should be noted that this approach, although promising, has not yet been validated with simulations of the expansions over time of exposure.

In the second approach, it is assumed that the volumetric strain (ε_v) is a result of the volume change associated with the chemical reactions involving calcium aluminate phases, ingressing sulfates, and ettringite formation. For any of the individual reactions described in Section 3.1, the volumetric change due to the difference in molar volumes between reactants and reaction products can be calculated using stoichiometric constants [16,52].

In this work, ettringite is assumed to be the only reaction product governing the expansion of the sample, and volumetric strains are obtained following the second approach. In this way, the volumetric change of the individual reactions is calculated as [52]:

$$\frac{\Delta V_i}{V_i} = \frac{V_f - V_i}{V_i} = \frac{m^{ettr} - m^i + a_i \cdot m^{gypsum}}{m^i + a_i \cdot m^{gypsum}} = \frac{m^{ettr}}{m^i + a_i \cdot m^{gypsum}} - 1 \qquad (18)$$

in which m^i is the molar volume (m^3/mol) of each species, and a_i is the stoichiometric coefficient involved in each reaction. It has been argued that the volume of water should enter the calculation of volume change as a reactant [6,8], which would lead to a volume reduction instead to an expansion. This is the main reason why this approach has been discarded by some researchers. However, to the authors' opinion, in external sulfate attack tests, where saturated samples are immersed in a sulfate solution, water supply may be considered as unlimited and instantaneous (as compared to the reaction speed of the sulfate attack) at the local level, and thus

should not enter the calculation of expansions, as the same amount of water may be considered to be present throughout the process. Indeed, since the ettringite penetration depth is usually in the millimeter range, it can be assumed that this layer will remain fully saturated throughout the test.In order to calculate the total volumetric strain, it is necessary to compute the amount of aluminate phases that have reacted (C_i^{react} or C_{eq}^{react} for the extended and simplified model, respectively). For the extended version of the model, it yields

$$\varepsilon_v = \sum_{i=1}^{n} C_i^{react} \frac{\Delta V_i}{V_i} \bar{m}^i - f \cdot \Phi_{ini} \tag{19}$$

with

$$\bar{m}^i = m^i + a_i \cdot m^{gypsum}\ (\mathrm{m^3/mol}), \text{and } C_i^{react} = C_i^0 - C_i^{unr}, \quad \text{for } i = 1, n \tag{20}$$

In the previous equations, C_i^0 is the initial concentration of the different aluminate phases, and C_i^{unr} is the respective unreacted amount (updated values of the internal variables). The second term in the RHS of Eq. (19) is introduced in order to account for the fact that not all of the ettringite formed will translate into expansions of the specimen. Instead, most of the models consider that a fraction f of the capillary porosity has to be filled before any expansion is observed [6,16,52].

For the simplified model, an averaging scheme is again used for the different phases, yielding

$$\varepsilon_v = \alpha_s \cdot C_{eq}^{react} - f \cdot \Phi_{ini} \tag{21}$$

with

$$\alpha_s = \sum_{i=1}^{n} \frac{\Delta V_i}{V_i} \cdot \bar{m}^i \cdot \frac{C_i}{\sum_j C_j}\ (\mathrm{m^3/mol}) \tag{22}$$

Typical values of parameter f in Eqs. (19) and (21) needed to fit experimental data are in the range 0.05–0.40 [52]. The dispersion of these values suggest that assuming that a fraction of the capillary porosity has to be filled before any expansion is observed may be rather arbitrary and could therefore be questionable.

In marked contrast, it has been suggested that ettringite crystals precipitate also (and mainly) intimately mixed with the C–S–H phase (in the gel porosity), as in the case of delayed ettringite formation (e.g. [8,50]). In this scenario, it is thought that the main cause of expansions is expected to be the ettringite that precipitates within the C–S–H phase (and the fraction that precipitates in the capillary pores does not have a significant contribution to the overall expansion). The proportion of ettringite growing within the C–S–H to that precipitating in the capillary pores would not necessarily have to remain constant in time, but would depend on factors like pore size distribution, connectivity of the pore network, etc. [20]. Although this hypothesis is different from the one adopted in most of the models proposed so far, including the one proposed in this paper, the mathematical treatment in both cases may not differ significantly, except that in the later case the threshold term may not be a constant, as in the present model, but a complex function of several variables, as mentioned above.

Despite the previous considerations, and until a clearer idea of the involved mechanisms is generally accepted, it has been decided in this work to maintain the formulation described by Eqs. (19)–(22), mainly because the model, while being simpler, yields very reasonable approximations, as will be shown in the following section.

From a numerical point of view, the chemo-mechanical coupling is achieved in the present paper through a staggered approach, as shown schematically in Fig. 4. One code (DRACFLOW) performs the nonlinear diffusion–reaction analysis, and the results in terms of local expansions serve as input to the second code (DRAC), solving the mechanical problem. The updated displacement field obtained in the latter will in turn alter the diffusion–reaction process in case that cracking occurs, as sulfate ingress will be accelerated due to cracking. As a result, this loop must be successively repeated within each time step until a certain tolerance is satisfied.

4. Results of the simulations

4.1. Comparison between coupled and uncoupled analyses

As a first step, the effect of coupling in the model when cracking occurs has been evaluated through an academic example of a small concrete specimen subjected to external sulfate attack. To this end, coupled and uncoupled simulations have been performed with the same FE mesh, with a cross-section of $6 \times 6\ \mathrm{cm^2}$ and a 4×4 aggregate arrangement (26% volume fraction and 15 mm of maximum aggregate size). The four faces of the specimen are exposed to a sodium sulfate solution with a fixed concentration (U_{imp}) of 35.2 ($\mathrm{mol/m^3}$) (or 5% Na_2SO_4). For simplicity, the lumped-reaction version of the model has been assumed in this case. For the matrix phase, an initial concentration of 9.13 wt.% of C_3A in the cement (ϑ) has been considered, corresponding to a CEM I 52.5R cement [1]. Knowing the cement content of the matrix phase (representing mortar plus small aggregates), an initial concentration of C_3A ($\mathrm{mol/m^3}$) may be derived as [16]

$$C_3A\ (\mathrm{mol/m^3}) = \frac{\vartheta}{M^{C_3A}} \cdot v_c = \frac{\vartheta}{M^{C_3A}} \cdot \left(1 + \frac{\rho_c}{\rho_s} s/c + \frac{\rho_c}{\rho_w} w/c\right)^{-1} \tag{23}$$

in which v_c ($\mathrm{m^3/m^3}$ of material) is the volumetric fraction of cement in the concrete, ρ_c, ρ_s, ρ_w are respectively the densities of cement, aggregates and water, M^{C3A} (g/mol) is the molar weight of C_3A (269.9 g/mol), and s/c and w/c are the aggregate-to-cement and water-to-cement weight ratios, respectively. In order to calculate the aggregate weight content (s), the fraction of aggregates explicitly discretized in the mesh has to be deducted from the total amount in the concrete.

Material parameters considered for the diffusion–reaction analysis in the two cases are as follows: $D_1 = 1.96 \times 10^{-12}$ ($\mathrm{m^2/s}$) (1.7×10^{-3} ($\mathrm{cm^2/day}$)), $k = 0.92 \times 10^{-9}$ ($\mathrm{m^3/(mol\ s)}$) (7.95×10^{-5} ($\mathrm{m^3/(mol\ day)}$)), $q = 3$, $f = 0.05$, $w/c = 0.5$, $\alpha = 0.9$, $D_0/D_1 = 0.05$, $\beta_D = 1.5$ and $\alpha_s = 1.133 \times 10^{-4}\ (\mathrm{m^3/mol})$. The effect of cracks on

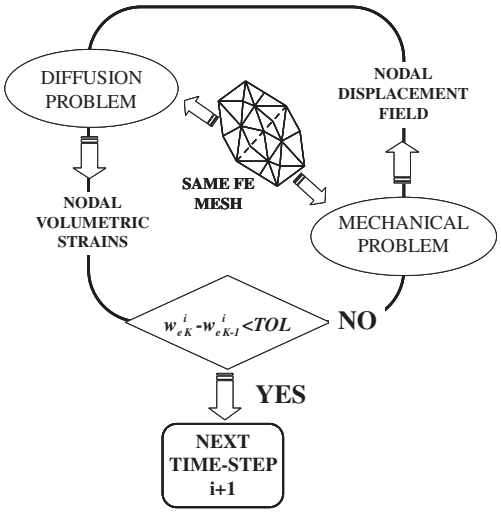

Fig. 4. Schematic representation of the hygro-mechanical staggered approach.

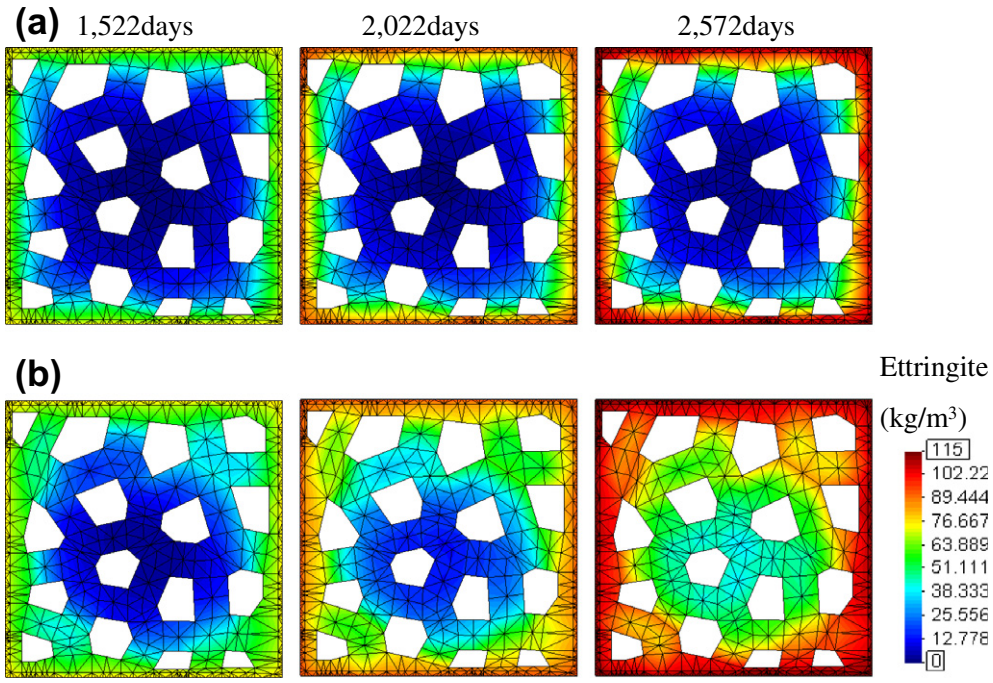

Fig. 5. Ettringite concentration (kg/m^3) for three different exposure times (1522, 2022 and 2572 days): (a) uncoupled and (b) coupled analyses. (For interpretation to colours in this figure, the reader is referred to the web version of this paper.)

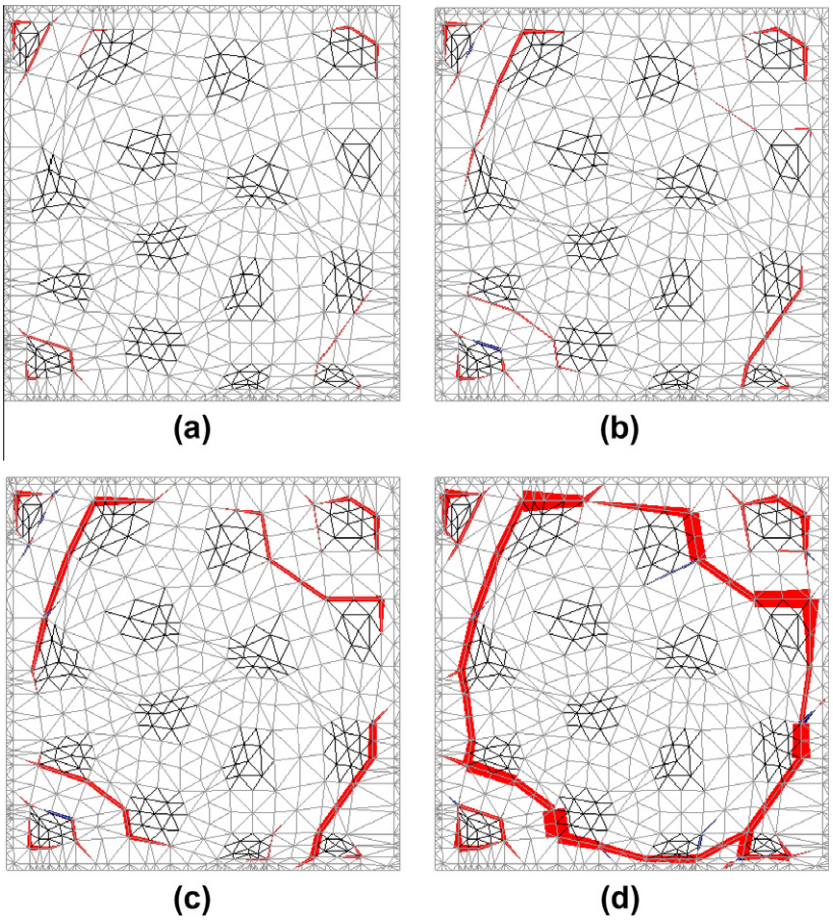

Fig. 6. Crack pattern evolution in terms of energy spent in the fracture process, for the following exposure times: (a) 672, (b) 722, (c) 772, and (d) 1022 days (until this point the results of the coupled and uncoupled analyses are almost equivalent). (For interpretation to colours in this figure, the reader is referred to the web version of this paper.)

the diffusion of sulfate ions is considered in the coupled simulations, assuming as a first step that the crack diffusivity is proportional to the cube of the crack width, with a parameter high enough to ensure a much more rapid diffusion through the crack

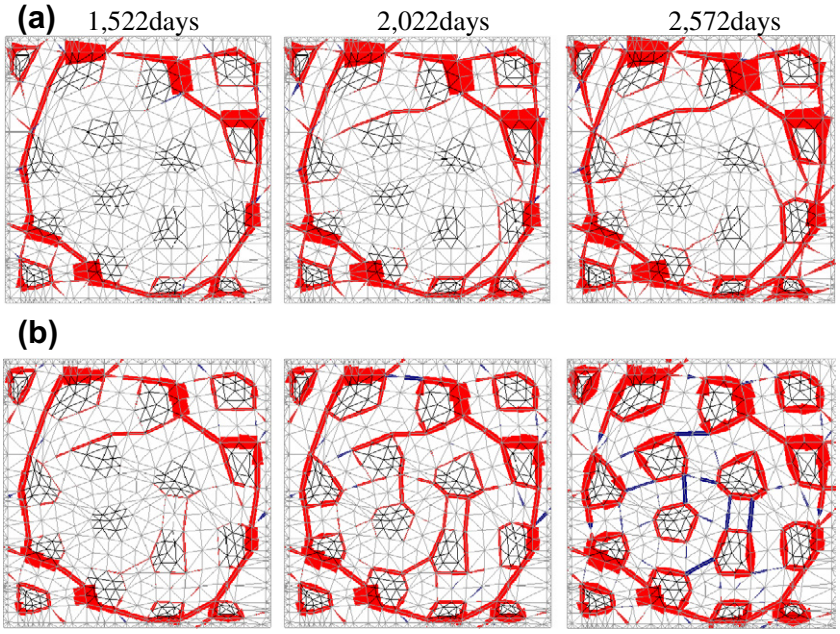

Fig. 7. Crack pattern evolution in terms of energy spent in fracture, showing spalling and micro-cracking around the aggregates: (a) uncoupled and (b) coupled cases at same exposure times of Fig. 5 (red = plastic loading; blue = elastic unloading). (For interpretation to colours in this figure, the reader is referred to the web version of this paper.)

than through the uncracked continuum. The model parameters for the mechanical analysis, not considering the aging effect and the viscoelastic behavior in this example, are the following: E_{aggr} = 70 GPa (aggregate elastic modulus), E_{matrix} = 25 GPa (matrix elastic modulus), ν = 0,2 (Poisson ratio for both continuum phases); for the aggregate–matrix interface elements: χ_0 = 2 MPa, c_0 = 7 MPa, tan ϕ_0 = 0.7, tan ϕ_r = 0.4, G_F^I = 0.03 N/mm, $G_F^I Ia = 10.G_F^I$, σ_{dil} = 40 MPa; for the matrix–matrix joint elements: same parameters, except χ_0 = 4 MPa, c_0 = 14 MPa, G_F^I = 0.06 N/mm, $G_F^I Ia = 10G_F^I$.

Fig. 5 depicts the results of the evolution of ettringite concentration (kg/m^3) for the: (a) uncoupled and (b) coupled cases, for three different advanced exposure times between 1522 and 2572 days (for which noticeable differences are observed between the two calculations). It may be noted that the front of ettringite formation, as a consequence of the penetration of the sulfate ions, advances with time towards the center of the specimen much faster in the coupled case, once cracking and spalling develop. Ettringite concentration is calculated from the reactions in Eq. (4): from each reacted mol of the aluminate phases a mol of ettringite is obtained (except for the C_4AF case).

In turn, Fig. 6 illustrates the evolution of the crack pattern in terms of the energy spent in the fracture process, for four different earlier exposure times between 672 and 1022 days (for which coupled and uncoupled analyses yield practically identical results). The open cracks (interface elements that have reached the initial cracking surface) are highlighted, in red if they are opening (plastic loading) or in blue if they are arrested (elastic unloading). The thickness of the color line represents the magnitude of the energy spent at each point. Cracking begins at the specimen corners, in the aggregate–matrix interfaces (Fig. 6a). These cracks evolve with increasing expansions, get connected through matrix cracks and eventually produce the spalling of a mortar layer, approximately at 1000 days of exposure, which can be seen in the figure as cracks parallel to the exposed surfaces, over the entire perimeter. Fig. 7 shows the evolution of the fracture process for the same exposure times of Fig. 5 for the: (a) uncoupled and (b) coupled cases. A correlation between the ettringite concentration results in Fig. 5 and the crack patterns shown in Fig. 7 is clearly observed. As soon as the corner cracks connect with the exposed surfaces, the coupled simulation accentuates the influence of these cracks as preferential penetration channels, leading to an increase of ettringite formation and thus to a higher level of expansions. In turn, a higher degree of internal micro-cracking between and around the aggregates is reached in the coupled case, as compared to the uncoupled one. The maximum crack width at 2572 days of exposure (located at the ring-shaped crack representing the spalling effect) is of 140 μm in the coupled case and 240 μm in the uncoupled one. A possible reason for this difference is depicted in Fig. 8, showing the ettringite concentration profiles at 2572 days for the two cases. It can be seen that in the uncoupled analysis, since the effect of cracks is not considered in the diffusion process, the ettringite profile has a more pronounced gradient near the exposed surfaces, thus causing excessive expansion of the outer layers and almost none in the interior of the sample. This is not the case in the coupled simulation, which shows a high ettringite content also in the interior of the sample, thus producing a more homogeneous expansion of the specimen, as compared to the uncoupled simulation.

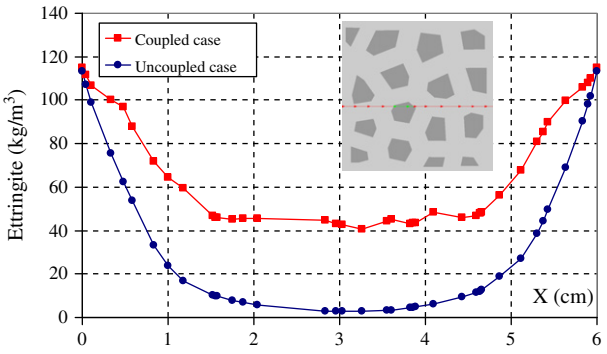

Fig. 8. Ettringite concentration (kg/m^3) profiles at 2572 days for the uncoupled and coupled analyses at the specified cross-section of the mesh. (For interpretation to colours in this figure, the reader is referred to the web version of this paper.)

Note that in the coupled analysis the internal cracking is much more pronounced when passing from 1522 to 2022 days of expo-

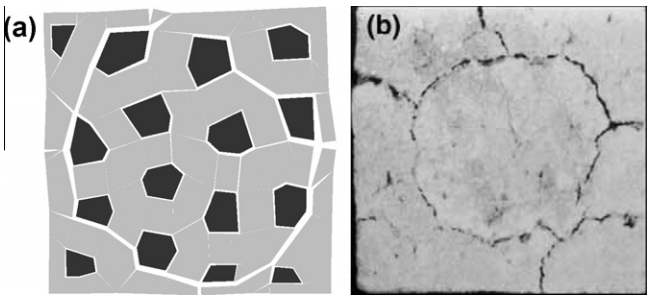

Fig. 9. Qualitative comparison between numerical and experimental crack patterns: (a) deformed mesh (scale factor = 8) and (b) typical cracks in a concrete sample (from [2], with permission of the author).

sure, and that from 2022 to 2572 days micro-cracking propagates around all the aggregates in the sample, representing the state of total disaggregation between matrix and aggregate. In addition, cracks propagating through the matrix (between neighboring aggregates) unload. The simulation captures the crack patterns and the spalling phenomena observed in lab experiments in a correct way, with the resulting reduction of effective area of the sample, and even the almost complete disintegration of the sample. This can be seen qualitatively in Fig. 9, in which the deformed mesh obtained in the simulation is compared to the final state of a real concrete sample (taken from [2]).

4.2. Influence of C_3A content

The influence of the C_3A content of the clinker on the resistance of concrete to sulfate attack is well-known, and has been traditionally used in the prescriptive design approach to prevent sulfate attack. A low C_3A content decreases the amount of aluminate phases in the hydrated cement paste, and therefore the potential to form ettringite, leading to significantly reduced expansions and cracking. Thus, as a second example, the influence of the initial C_3A content on the mechanical response has been studied with the same academic example of a $6 \times 6\ cm^2$ concrete specimen. To this end, another coupled simulation, in addition to the one presented in the previous section (with 9.13 wt.% of C_3A), has been performed considering a low C_3A content of 4.56 wt.%, corresponding to a CEM I 52.5N/SR sulfate-resistant cement [1], the rest of the parameters remaining identical to the previous example.

The results obtained regarding the mechanical response for the low and high C_3A cases are compared in Fig. 10, in terms of the energy spent in fracture. The figure shows the cracking state for the two kinds of cement, at four exposure times of 1022, 1522, 2022 and 2572 days. According to these results, the low C_3A cement would exhibit a much higher sulfate resistance, as manifested by a significant delay spalling of the concrete outer layer, which occurs approximately 3 years later than in the high C_3A content sample (from around 1022 to 2022 days). Note also that the interior core of the sample remains relatively unaltered in the low C_3A case.

4.3. Simulation of experiments on prismatic concrete samples

This section presents the results of the simulation of recent experiments of external sodium sulfate attack on concrete prisms [54]. In that work, a wide range of binder materials, including ordinary Portland concrete (OPC), were studied. In the present paper we only focus on OPC (ASTM Type I cement), for which the chem-

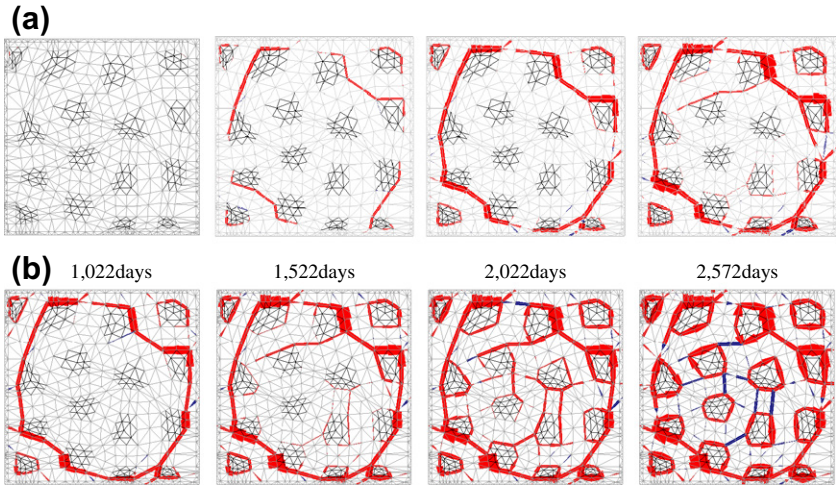

Fig. 10. Comparison of the crack pattern evolution, in terms of energy spent in fracture, for cases with: (a) low and (b) high C_3A initial content in the cement, at 1022, 1522, 2022 and 2572 days of exposure. (For interpretation to colours in this figure, the reader is referred to the web version of this paper.)

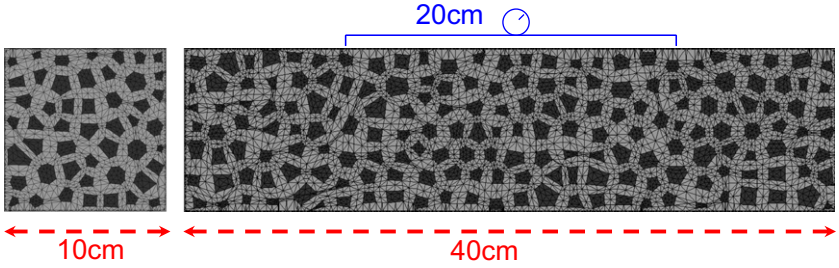

Fig. 11. Meshes used in the simulations for the cross-section (size is $10 \times 10\ cm^2$) and for the longitudinal section (size is $10 \times 40\ cm^2$) with a 20 cm strain measurement basis. (For interpretation to colours in this figure, the reader is referred to the web version of this paper.)

Table 1
Aluminate phases present in the cement before hydration and after 28 days of hydration, as calculated from thermodynamic modeling [31].

Condition	Aluminate phases (g/100 g unhyd. cem.)		
	C_3A	C_4AF	Afm
Unhydrated clinker	7.09	8.22	0
After 28 days of hydration	1.07	2.29	16.86

Table 2
Summary of the material parameters used in the simulations of the experiments on concrete specimens by [54].

Diffusion–reaction model (matrix)		Mechanical analysis (continuum)	
Material parameters for simulations of experiments by [54]			
Initial humidity	100%	E_{matrix} (GPa)****	26 (at 28 days)
D_0 (cm^2/day)	3.2×10^{-4}	E_{aggr} (GPa)	70
D_1 (cm^2/day)	1.6×10^{-3}	ν_{matrix}; ν_{aggr}	0.2; 0.2
β_D (–)	1.5	Mechanical analysis (joint elements)	
k (m^3/(mol day))	1.1×10^{-4}	χ (MPa)***	2.5; 5.0
$\alpha_{hydration}$	0.90	c (MPa)***	8.0; 16.0
w_0/c	0.50	tan ϕ, tan ϕ_{res}	0.7, 0.2
q^*; f	2.375; 0.10	G_F^I (N/mm)***	0.04; 0.08
α_s**	2.98×10^{-4}	$G_F^I Ia$ (N/mm)	$10 \times G_F^I$
Diffusion analysis (joint elements)		σ_{dil} (MPa)	40
$CA_{initial}$ (mol/m^3)*	202.08	p_χ, p_c, p_{GF}	0.4, 0.5, 0.8
U_0 (mol/m^3)	35.2	K_χ, K_c, K_{GF}	1.0, 1.0, 1.0

* Calculated as detailed in Section 3.2.
** Calculated with Eq. (22).
*** Aggregate–matrix; matrix–matrix interfaces.
**** Aging Maxwell-chain.

ical reactions involved and the degradation processes may be well represented by the model presented in this paper. Unfortunately, due to the complexity of the experimental quantification of ettringite profiles (see e.g. [53]), only the expansions and flexural strength were measured in that work.

Concrete prisms of $10 \times 10 \times 40$ cm^3 were cast and immersed in 5% Na_2SO_4 solution (sulfate concentration = 35.2 (mol/m^3)), and expansions were measured periodically during 224 days. Only the case with w/c ratio of 0.5 (cured for 28 days) has been simulated in this study since we are mainly interested in capturing the right trends and confirming that the model yields reasonable approximations. The experimental data of the tested concrete may be found in [23,54]. The maximum aggregate size used was 20 mm for the coarse fraction and 5 mm for the fines. In order to avoid the influence of the casting direction (e.g. warping of the samples, see [44]), expansions were experimentally measured on the side faces. The measurement basis is 20 cm and the average of four measurements for two prisms is considered in the results.

The meshes used in the simulations are shown in Fig. 11, with an aggregate volume fraction of 30% (maximum and minimum aggregate sizes: 16.5 mm and 5 mm, respectively), as deduced approximately from the mix-design data (the remaining volume fraction, i.e. with aggregate size smaller than 5 mm, is considered to be diluted in the matrix). One of the meshes has dimensions 10×40 cm^2, in order to calculate the longitudinal expansions, with a central measurement basis of 20 cm. Additionally, a cross-section of the prism has been considered (size is 10×10 cm^2) to follow its degradation, accounting for the corner effects. A third mesh of 10×20 cm^2, corresponding to the central part of the 10×40 cm^2 mesh, has been generated by cutting the previous mesh and enforcing the end faces to remain planar (so that it represents the same mechanical behavior with a measurement basis of 20 cm). Expansions were measured as the average of the longitudinal strains of the top and bottom faces of the mesh, with the 20 cm basis (centered).

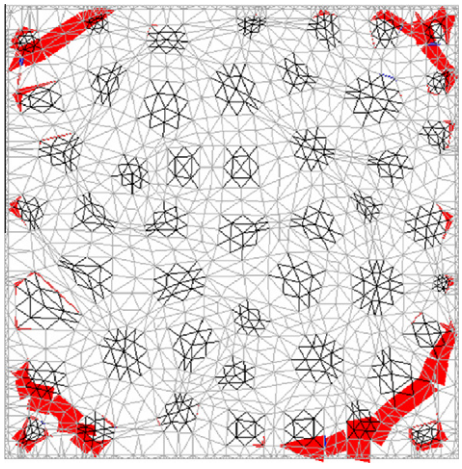

Fig. 12. Simulation results of cracking in a section of the concrete specimen (in terms of energy spent in fracture, red = plastic loading; blue = elastic unloading). (For interpretation to colours in this figure, the reader is referred to the web version of this paper.)

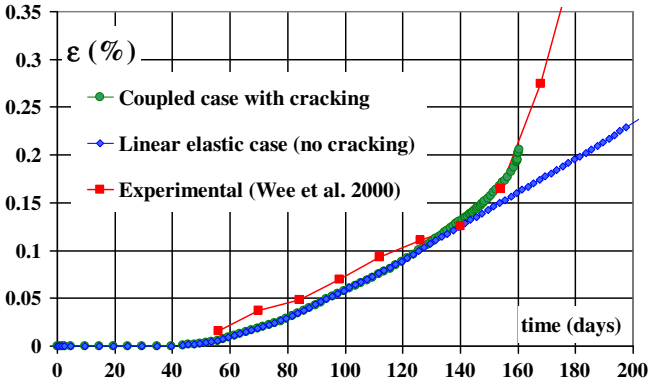

Fig. 13. Comparison of the evolution of longitudinal expansions with time of exposure to a Na_2SO_4 solution: experimental and numerical results (with and without interface elements). (For interpretation to colours in this figure, the reader is referred to the web version of this paper.)

As a first approximation of the distribution of the different aluminate phases of the hydrated cement in the simulations, a hydrated phase assemblage at 28 days for a similar CEM I OPC has been adopted from previous calculations based on thermodynamic modeling [31]. It is noted that even though the oxide composition of the cements is similar in both cases, there is no data on the Blaine surface area and CO_2 content of the cement used by [54], which would be needed for a more accurate prediction. In this way, part of the initial C_3A and C_4AF are hydrated mainly into monosulfoaluminate (AFm phase), as shown in Table 1. The adopted values were calculated using thermodynamic modeling of the phase assemblage at equilibrium, using the freely available geochemical code GEMS-PSI [25], coupled to a set of simple equations to describe the kinetics of cement hydration [36], and a specific thermodynamic database for cementitious systems [33].

Additionally, the results from thermodynamic modeling in [31] have been exploited to estimate the evolution due to hydration of the expansion coefficient (α_s) given by Eq. (22). This expression has been evaluated at different hydration times (the relation between the different aluminate phases in the cement evolves with hydration). The results have shown that the variation with respect to the value of α_s at 28 days is less than 10%, thus supporting the idea of using a constant expansion coefficient value, which is equal to 2.98×10^{-4} m^3/mol in the present case.

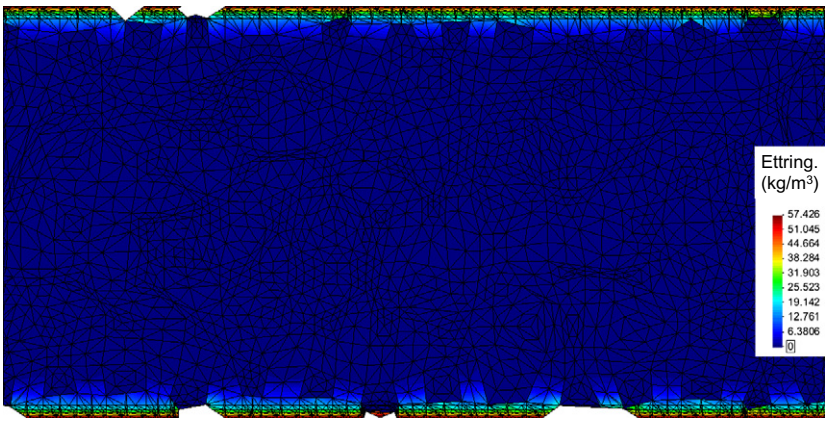

Fig. 14. Ettringite concentration in the matrix phase at 160 days of exposure, showing precipitation only near the exposed surface, within the first 4–6 mm depth. Note the effect of spalled layers on the ettringite concentration. (For interpretation to colours in this figure, the reader is referred to the web version of this paper.)

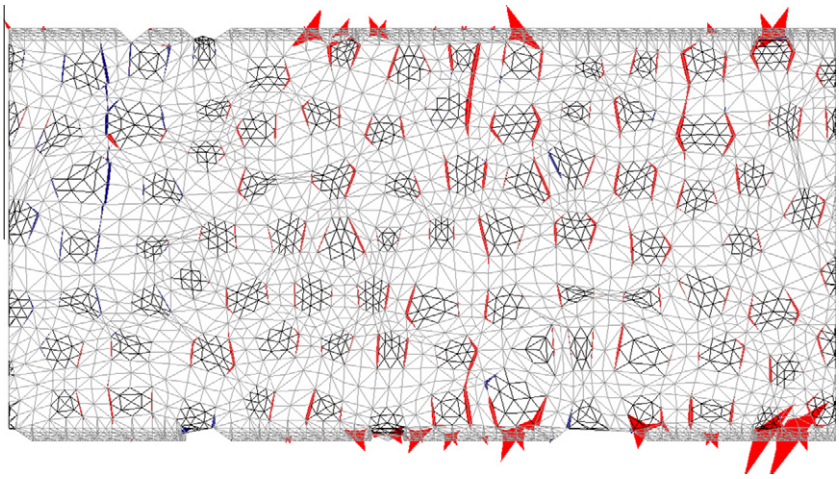

Fig. 15. Crack pattern at 160 days of exposure for the central 20 cm of the specimen, in terms of energy spent in fracture, showing incipient internal cracking and spalled layers. (For interpretation to colours in this figure, the reader is referred to the web version of this paper.)

The parameters finally used in the simulations are gathered in Table 2. The initial concentration of equivalent alumina ($CA_{initial}$ in Table 2) has been calculated from data in Table 1 (molar weights were extracted from GEMS database), and taking into account the aggregate volume fraction that has not been discretized in the FE mesh. Parameters q and α_s have been calculated from the expressions in Section 3.2, while parameters f, k and D_1 have been fitted to the experimental results (the remaining ones are either input test data or estimated from the concrete composition).

Fig. 12 shows the state of the cross-section (end face) of the simulated cross-section, in terms of the energy spent in the fracture process in the interface elements. As in the experiments (see [54], cracking is observed at the corners, although in the experiments the spalled layer is larger. This could be due to the fact that the photograph in [54] has been taken on the end face of the sample, where the degradation is maximal. This aspect cannot be considered with the present two-dimensional simulation. A more accurate comparison of these degraded surfaces would require a full 3D analysis, which is out of the scope of the present study.

The longitudinal expansions obtained in the simulations are also compared with the experimental measurements in Fig. 13. In the figure, two numerical curves are included, the one obtained with the full-fetched model including cracking and chemo-mechanical coupling effects, and a simplified one without interface elements (and therefore without cracking or coupling). The numerical curves show both an increase of the expansions rate until around 90 days, which is due exclusively to the increase of the ettringite penetration depth: the thicker the expansive ettringite layer, the larger the overall expansion rate. However, only the model with interface elements can capture the significant increase in expansion rate caused by cracking around 120 days, while the model without interfaces maintains a constant expansion rate, thus not representing this effect.

In Fig. 14, the ettringite concentration is presented, showing that even at an advanced state of exposure the penetration front of ettringite precipitation concentrates in the first 4–5 mm. In the figure, some spalling along the upper and lower surfaces of specimen is apparent. The spalled elements were removed from the calculation as all the interfaces around them were totally fractured. As the elements were removed, the new boundaries for diffusion of sulfate ions were modified accordingly, although this is not fully reflected in the ettringite due to the time lag imposed by the reaction kinetics. Accordingly, Fig. 15 depicts the energy spent in fracture processes at the interface elements (red = plastic loading; blue = elastic unloading) for the same time of exposure as in Fig. 14. It can be observed that the most developed cracks are near the surface, indicating further potential spalling. Also, the model predicts incipient but important micro-cracking across the entire concrete specimen inherent of the mesostructural representation, nucleating mainly along the vertical parts of the aggregate–matrix interfaces, even if the expansive reaction products are limited to the surface of the specimen. These remarkable features

of the numerical results presented are consistent with experimental observations in different concretes, for which large expansions, important cracking and spalling phenomena are observed even for ettringite penetration depths of the order of a few millimeters, whereas the sample sizes are of the order of several centimeters (see e.g. [15,45]).

5. Concluding remarks

A chemo-mechanical (C-M) FE model for concrete subjected to external sulfate attack at the meso-level has been presented. A basic underlying assumption of the meso-level analysis is that the main aspects of the mechanical behavior as well as cracking and degradation due to diffusion-driven phenomena may be captured by only representing the largest aggregate pieces while the rest (smaller aggregates and sand) are considered to be represented by the 'matrix' phase. Cracking is introduced via zero-thickness interface elements equipped with an elasto-plastic fracture-based constitutive law, and the additional ion diffusion through open cracks is explicitly accounted for in the simulations. The chemo-transport model is based on the formulation proposed in [52], with some new features proposed in this paper, as the explicit diffusion through open cracks, the possibility of considering different kinetics for each chemical reaction, or the dependence of the diffusion coefficient of the uncracked continuum media on the capillary porosity (based on an hyperbolic law), which decreases due to ettringite precipitation in the pores. The resulting model seems capable of capturing the key aspects of external sulfate attack on concrete specimens as observed in laboratory experiments.

In particular, it has been shown that the effect of coupling (effect of cracks on reactive transport process) is very important in the case of external sulfate attack, due in part to the magnitude of the maximum crack widths found in the spalled layer, which are of the order of 100–200 μm. Cracks represent preferential penetration channels for the diffusion of sulfates into the sample. In turn, the acceleration of the diffusion–reaction process leads to a higher degree of mechanical degradation, with wider cracks around and between the aggregates, eventually leading to the disintegration of the sample. As a consequence, the penetration of sulfate ions is much more pronounced than in the uncoupled analysis. None of the models proposed in the literature seem to be able to capture the main crack patterns correctly, nor are they able to account for the effect of cracking and spalling on the transport processes.

The effect of the C_3A content in the cement has been studied at the meso-scale for the case of concrete. The results show lower levels of expansion on mortar prisms as determined experimentally and an important retardation of the cracking process in the low C_3A concrete specimen as compared to the high C_3A content sample, suggesting a much higher resistance to external sulfate attack in the former case.

Finally, recent experiments on concrete prisms subjected to a sodium sulfate solution [54] have been simulated with the present model showing a reasonable approximation of the longitudinal expansions over time of exposure.

The development of the coupled C-M model presented has left some open topics for future improvements. In this paper, the coupling with leaching has not been pursued. Thus, the increase in porosity (and eventual loss of stiffness) due to portlandite dissolution has not been considered in the present model. In order to introduce this effect, a multi-ionic diffusion–reaction model should be considered (see e.g. [32]). Another simplification is the fact that the elastic modulus of the continuum matrix phase is unaffected by the chemical degradation process (the overall stiffness is only affected by crack propagation). To account for this effect, a damage model (with the consequent regularization problems) or a homogenized scheme for the variable mechanical properties of the matrix should be included in the analysis. However, more experimental data on this matter than available at present would be needed to verify such degradation process. The need for extending the analysis to the 3D case has also been noticed. Its consideration would allow the representation of any type of boundary conditions. Moreover, the limitations arising from the 2D representation of specimen and aggregates geometries can only be totally overcome with a full 3D analysis. Finally, the possibility of coupling the transport-mechanical model with an existing code for thermodynamic modeling of the phase assemblage at equilibrium (e.g. [25]) could be also explored.

Acknowledgements

This research has been supported by grants BIA2006-12717 funded by MEC (Madrid, Spain) and BIA2009-10491 funded by MICINN (Madrid, Spain), as well as grant 2009SGR-180 from AGAUR-Generalitat de Catalunya, Barcelona). The first author also wishes to thank MEC for the FPI doctoral fellowship (2004-2008). Special thanks to Dr. Barbara Lothenbach (EMPA, Switzerland) and Prof. Ignasi Casanova (UPC, Spain) for insightful discussions.

References

[1] Akpinar P. Multi-approach studies on the mechanisms of sulfate-induced degradation of cementitious materials. PhD thesis, UPC, Barcelona, Spain, 2006.
[2] Al-Amoudi OSB. Attack on plain and blended cements exposed to aggressive sulfate environments. Cem Concr Compos 2002;24:305–16.
[3] Bary B. Simplified coupled chemo-mechanical modeling of cement pastes behavior subjected to combined leaching and external sulfate attack. Int J Numer Anal Meth Geomech 2008;32:1791–816.
[4] Bary B, Béjaoui S. Assessment of diffusive and mechanical properties of hardened cement pastes using a multi-coated sphere assemblage model. Cem Concr Res 2006;36:245–58.
[5] Basista M, Weglewski W. Micromechanical modelling of sulphate corrosion in concrete: influence of ettringite forming reaction. Theor Appl Mech 2008;35:29–52.
[6] Basista M, Weglewski W. Chemically assisted damage of concrete: a model of expansion under external sulfate attack. Int J Damage Mech 2009;18:155–75.
[7] Bazant ZP, Panula L. Practical prediction of time-dependent deformations of concrete. Part II: basic creep. Mater Struct 1978;11:317–28.
[8] Brown P, Taylor H. The role of ettringite in external sulfate attack. In: Marchand, Skalny, editors. Mat. Science of Concrete: Sulfate Attack Mech.. Amer. Cer. Soc. Press; 1998. p. 73–98.
[9] Caballero A. 3D meso-mechanical numerical analysis of concrete fracture using interface elements. PhD thesis, UPC, Barcelona, Spain, 2005.
[10] Caballero A, López CM, Carol I. 3D meso-structural analysis of concrete specimens under uniaxial tension. Comput Meth Appl Mech Eng 2006;195:7182–95.
[11] Caballero A, Carol I, López CM. 3D meso-mechanical analysis of concrete specimens under biaxial loading. Fatigue Fract Eng Mater Struct 2007;30:877–86.
[12] Carol I, Prat P, López CM. Normal/shear cracking model. Application to discrete crack analysis. ASCE J Eng Mech 1997;123:765–73.
[13] Carol I, López CM, Roa O. Micromechanical analysis of quasi-brittle materials using fracture-based interface elements. Int J Numer Meth Eng 2001;52:193–215.
[14] Carol I, Idiart AE, López CM, Caballero A. Multiaxial behavior of concrete. A mesomechanical approach. Rev Eur Genie Civil 2007;11:907–26.
[15] Chabrelie A. Mechanisms of degradation of concrete by external sulfate ions under laboratory and field conditions. PhD thesis, EPFL, Lausanne, Switzerland; 2010.
[16] Clifton JR, Pommersheim JM. Sulfate attack of cementitious materials: volumetric relations and expansions. NISTIR 5390, NIST; 1994.
[17] Cohen MD. Theories of expansion in sulfoaluminate-type expansive cements: schools of thought. Cem Concr Res 1983;13:809–18.
[18] Djerbi A, Bonnet S, Khelidj A, Baroghel-Bouny V. Influence of traversing crack on chloride diffusion into concrete. Cem Concr Res 2008;38:877–83.
[19] EHE, Instrucción de Hormigón Estruct. EHE. Min. de Fomento, Madrid; 1998 [in Spanish].
[20] Flatt RJ, Scherer GW. Thermodynamics of crystallization stresses in DEF. Cem Concr Res 2008;38:325–36.
[21] Garboczi EJ, Bentz DP. Computer simulation of the diffusivity of cement-based materials. J Mater Sci 1992;27:2083–92.
[22] Gospodinov P, Kazandjiev R, Miranova M. The effect of sulfate ion diffusion on the structure of cement stone. Cem Concr Compos 1996;18:401–7.

[23] Idiart AE. Coupled analysis of degradation processes in concrete specimens at the meso-level. Doctoral Thesis, UPC, Barcelona, Spain; 2009.
[24] Idiart AE, López CM, Carol I. Modeling of drying shrinkage of concrete specimens at the meso-level. Mater Struct. doi:10.1617/s11527-010-9636-2.
[25] Kulik D. GEMS-PSI 2.3.0, PSI-Villigen, Switzerland; 2009. <http://gems.web.psi.ch/>.
[26] Lee S, Hooton R, Jung H, Park D, Choi C. Effect of limestone filler on the deterioration of mortars and pastes exposed to sulfate solutions at ambient temperature. Cem Concr Res 2008;38:68–76.
[27] López CM, Carol I, Murcia J. Mesostructural modeling of basic creep at various stress levels. In: Ulm, Bazant, Wittmann, editors. Creep, Shrinkage & Durab. Mech. Concr. other quasi-brittle Mat. (Concreep6), Cambridge, USA; 2001. p. 101–6.
[28] López CM, Segura JM, Idiart AE, Carol I. Mesomechanical modeling of drying shrinkage using interface elements. In: Pijaudier-Cabot, Gérard, Acker, editors. Creep, Shrink Durab Concr & Concr Struct. (Concreep7), Nantes, France; 2005. p. 107–12.
[29] López CM, Carol I, Aguado A. Meso-structural study of concrete fracture using inter-face elements. I: numerical model and tensile behavior. Mater Struct 2008;41:583–99.
[30] López CM, Carol I, Aguado A. Meso-structural study of concrete fracture using inter-face elements. II: compression, biaxial and Brazilian test. Mater Struct 2008;41:601–20.
[31] Lothenbach B, Le Saout G, Gallucci E, Scrivener K. Influence of limestone on the hydration of Portland cements. Cem Concr Res 2008;38:848–60.
[32] Marchand J, Samson E, Maltais Y, Beaudoin J. Theoretical analysis of the effect of weak sodium sulfate solutions on the durability of concrete. Cem Concr Compos 2002;24:317–29.
[33] Matschei T, Lothenbach B, Glasser FP. Thermodynamic properties of Portland cement hydrates in the system $CaO–Al_2O_3–SiO_2–CaSO_4–CaCO_3–H_2O$. Cem Concr Res 2007;37:1379–410.
[34] Monteiro PJM, Kurtis KE. Time to failure for concrete exposed to severe sulfate attack. Cem Concr Res 2003;33:987–93.
[35] Neville AM. Properties of concrete. 4th ed. Pearson Prentice Hall; 2002.
[36] Parrot LJ, Killoh DC. Prediction of cement hydration. Brit Ceram Proc 1984;35:41–53.
[37] Ping X, Beaudoin JJ. Mechanism of sulphate expansion II. Validation of thermodynamic theory. Cem Concr Res 1992;22:845–54.
[38] Planel D. Les effets couplés de la précipitation d'espèces secondaires sur le comportement mécanique et la dégradation chimique des bétons. PhD thesis, Univ. Marne-la-Vallée, France; 2002 [in French].
[39] Samson E, Marchand J. Modeling the transport of ions in unsaturated cement-based materials. Comput Struct 2007;85:1740–56.
[40] Samson E, Marchand J, Snyder K. Calculation of ionic diffusion coefficients on the basis of migration test results. Mater Struct 2003;36:156–65.
[41] Santhanam M, Cohen MD, Olek J. Sulfate attack research – whither now? Cem Concr Res 2001;31:845–51.
[42] Santhanam M, Cohen MD, Olek J. Mechanism of sulfate attack: a fresh look. Part 1: summary of experimental results. Cem Concr Res 2002;32:325–32.
[43] Sarkar S, Mahadevan S, Meeussen JCL, van der Sloot H, Kosson DS. Numerical simulation of cementitious materials degradation under external sulfate attack. Cem Concr Compos 2010;32:241–52.
[44] Schmidt T. Sulfate attack and the role of internal carbonate on the formation of thaumasite. PhD thesis, EPFL, Lausanne, Switzerland; 2007.
[45] Schmidt T, Lothenbach B, Romer M, Neuenschwander J, Scrivener K. Physical and microstructural aspects of sulfate attack on ordinary and limestone blended Portland cements. Cem Concr Res 2009;39:1111–21.
[46] Schmidt-Döhl F, Rostásy F. A model for the calculation of combined chemical reactions and transport processes and its application to the corrosion of mineral-building materials Part I. Simulation model. Part II. Experimental verification. Cem Concr Res 1999;29:1039–53.
[47] Segura JM, Carol I. On zero-thickness interface elements for diffusion problems. Int J Numer Anal Meth Geomech 2004;28(9):947–62.
[48] Shazali M, Baluch M, Al-Gadhib A. Predicting residual strength in unsaturated concrete exposed to sulfate attack. ASCE J Mater Civil Eng 2006;18:343–54.
[49] Skalny J, Marchand J, Odler I. Sulfate attack on concrete. Spon Press; 2002.
[50] Taylor H, Famy C, Scrivener K. Delayed ettringite formation. Cem Concr Res 2001;31:683–93.
[51] Tian B, Cohen MD. Does gypsum formation during sulfate attack on concrete lead to expansion? Cem Concr Res 2000;30:117–23.
[52] Tixier R, Mobasher B. Modeling of damage in cement-based materials subjected to external sulfate attack. I: formulation. II: comparison with experiments. ASCE J Mater Civil Eng 2003;15:305–22.
[53] Wang JG. Sulfate attack on hardened cement paste. Cem Concr Res 1994;24:735–42.
[54] Wee TH, Suryavanshi AK, Wong SF, Anisur Rahman AK. Sulfate resistance of concrete containing mineral admixtures. ACI Mater J 2000;97(5):536–49.